Wave-matching-method for mode analysis of dielectric waveguides

*Manfred Lohmeyer**

Department of Physics, University of Osnabrück, Germany

Abstract: Frequently the cross section of a longitudinally homogeneous dielectric waveguide may be decomposed into rectangles with constant permittivity. For points inside these rectangles the wave equation for modal fields is solved analytically by expanding into functions with harmonic or exponential dependence on the transverse coordinates. Minimization of a least squares expression for the remaining misfit on the boundary lines allows us to determine propagation constants and fields for guided modes. Semivectorial calculations for two sets of rib waveguides and the center sections of a directional coupler and a MMI device show very good agreement with results found in the literature.

Keywords: integrated optics, dielectric waveguides, guided modes, numerical modeling

1 Introduction

Accurate calculation of modal fields and propagation constants is one of the principal tasks of numerically simulating integrated optical devices. A large variety of computational methods have been proposed, [1, 2] give an overview. There are a few approximative analytical approaches towards the problem (e.g. [3, 4, 5, 6, 7, 8, 9]). While being quite economical with computational resources, their applicability is limited by the approximations they rely on. More versatile, but computationally more expensive methods are usually based on finite element or finite difference approximations of Maxwells equations (e.g. [10, 11, 12, 13, 14, 15, 16, 17, 18, 19, 20, 21]), some using beam propagation techniques (e.g. [22, 23, 24, 25, 26]). Others expand the electromagnetic fields into sets of orthogonal functions (e.g. [27, 28, 29, 30]), [31] suggests a mixture of both.

Waveguides in integrated optics are formed either by a diffusion or an etching process. In the first case the refractive index varies smoothly in the substrate region, in the second case the guiding profile shows sharp discontinuities with constant permittivity in-between. Most examples in the above mentioned articles refer to waveguides of the second type, but most of the more rigorous methods do not exploit this feature. Our approach is based on it.

As a motivation, recall the common way to calculate propagation constants and modal fields of a *planar* slab waveguide with stepwise constant refractive index profile. Three steps have to be performed. First, for each slab, one has to write the modal field as a sum of physically reasonable fundamental solutions of the wave equation. Second, the continuity requirements for the electromagnetic fields must be incorporated to connect the unknown coefficients on neighboring slabs, resulting in a system of linear equations. Third, this system has to be solved for a nonvanishing field. We tried to establish an analogous procedure for two transverse dimensions.

The paper is organized as follows. In the next section we introduce some notation and recall the basic relations for semivectorial modal fields. In section 3 suitable fundamental solutions are set up, separately for each region with constant refractive index. Since the number of these trial functions is not limited, one has to select. Therefore the method cannot be expected to give exact results as in the planar case, and the way to connect different regions and the solution method have to be modified. We adopted a least squares method similar to [32], see section 4. The resulting numerical procedure to determine guided modes is the subject of section 5. The last main section reports on sample calculations for several rib waveguide stuctures and compares with results of other methods. For this purpose, we refer to the present approach as "wave matching method" WMM.

---

* *Fachbereich Physik, Universität Osnabrück*   *Barbarastraße 7, D 49069 Osnabrück*
Tel.: +541/969-2641   Fax: +541/969-2670   e-mail: manfred.lohmeyer@physik.uni-osnabrueck.de

2 Equations for guided modes

Consider a longitudinally homogeneous dielectric waveguide prescribed by a permittivity profile which can be divided into rectangles with constant refractive index. The z-axis denotes the direction of propagation, the transverse (x, y) axes are parallel to the refractive index discontinuities. Fig. 1 shows a typical example.
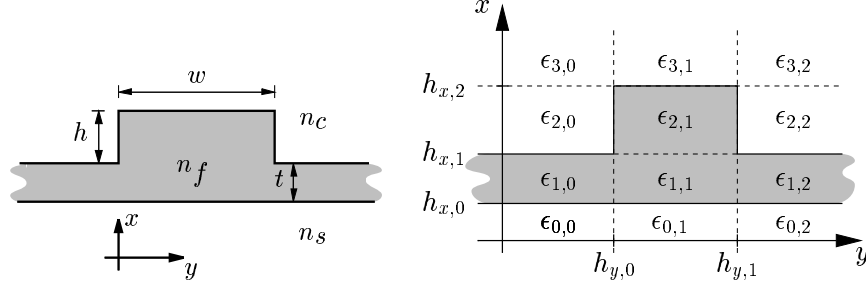

Figure 1: Sample structure: The cross section of a rib waveguide can be divided into 12 rectangles with constant permittivity. Note that the first and last rectangles in each horizontal and vertical slice are unbounded. n_s, n_f, n_c: refractive indices of the substrat, film and cover layer, h, w: rib height and width, t: remaining film thickness.

The waveguide cross section consists of $(N_x + 2) \times (N_y + 2)$ rectangles with diagonal isotropic permittivity $\epsilon^{lm} = (n^{lm})^2$, $l = 0, \ldots, N_x + 1$, $m = 0, \ldots, N_y + 1$, separated by the horizontal lines $x = h_{x,l}$, $l = 0, \ldots N_x$ and vertical lines $y = h_{y,m}$, $m = 0, \ldots N_y$. The superscript r will be used to shorthand denote a rectangle l, m. All electromagnetic field components F are of the form

$$F(x, y, z, t) = \Phi(x, y) \, e^{i(\omega t - \beta z)}, \tag{1}$$

where $\omega = kc = 2\pi c/\lambda$ is the angular frequency corresponding to the vacuum wavelength λ and speed of light c. Inserted into Maxwell's equations, this ansatz yields the following equation for the components Φ of the modal fields and the propagation constant β:

$$\partial_x^2 \Phi + \partial_y^2 \Phi = (\beta^2 - k^2 \epsilon^r)\Phi. \tag{2}$$

It is valid for all points *inside* rectangle r and has to be supplemented by suitable continuity relations on the boundaries. We restrict ourselves to the semivectorial treatment [12, 13], assuming that replacing $\partial_y \epsilon$ by $\epsilon \partial_y$ is a good approximation at least for the modes under consideration. Typically, y is along the substrate surface, the direction in which the field is less tightly confined.

For so called Quasi-TE polarization (QTE), consider the electric field component E_y. The second transversal component E_x is assumed to vanish. On horizontal boundaries, E_y and its normal derivative $\partial_x E_y$ ($\sim H_z$) must be continuous. On vertical boundaries, continuity is required for the product ϵE_y (the normal component of the dielectric displacement) and the derivative $\partial_y E_y$ ($\sim E_z$). In general there is a discontinuity in E_y on the lines $y = h_{y,m}$.

For Quasi-TM polarization (QTM), we use the y-component H_y of the magnetic field, setting H_x to zero. On horizontal boundaries, H_y and the product $\epsilon^{-1}\partial_x H_y$ ($\sim E_z$) must be continuous, while on vertical boundaries both the field H_y and its normal derivative $\partial_y H_y$ ($\sim H_z$) have to be continuous.

A guided mode is found if one can write down a square integrable field Φ which satisfies Eq. (2) inside the rectangles and the continuity requirements on their boundaries. This will be possible only for a certain number of discrete propagation constants β.

To calculate them we implemented the following procedure. For a trial value β, one picks that field from a given superposition of solutions to Eq. (2) which meets the boundary conditions best. Near a propagation constant the remaining violation of continuity requirements is expected to be minimal with respect to β. The minimum identifies the estimate for the propagation constant; the corresponding optimal trial function approximates the modal field.

3 Trial functions

On each rectangle r, the modal field Φ is assumed to be a linear combination of J^r trial functions ϕ_j^r:

$$\Phi(x,y) = \Phi^r(x,y) \quad \text{if } (x,y) \in \text{rectangle } r, \quad \text{with} \quad \Phi^r(x,y) = \sum_{j=0}^{J^r-1} a_j^r \phi_j^r(x,y) \,. \tag{3}$$

The unknown amplitudes a_j^r will be subject of the subsequent computation.

Since Eq. (2) and the boundary conditions are real linear relations, their solutions can be chosen real as well. We specialize to functions which factorize with respect to the transverse coordinates:

$$\phi_j^r(x,y) = c_j^r F_j^r(p_j^r(x - x_{0,j}^r)) \cdot G_j^r(q_j^r(y - y_{0,j}^r)). \tag{4}$$

$x_{0,j}^r$, $y_{0,j}^r$ are local coordinate offsets and c_j^r is a normalization constant (see below). For the rest of this section we suppress the label r of the rectangle under consideration.

ϕ_j satisfies Eq. (2) for $F_j, G_j \in \{\cos, \sin, \exp\}$, if an identity

$$\pm(p_j)^2 \pm (q_j)^2 = \beta^2 - k^2\epsilon \tag{5}$$

holds for the transverse wave vector components p_j, q_j. The signs depend on whether $\sin, \cos$ or $\exp$ was chosen for F_j and G_j.

Now for each rectangle r and trial value β a reasonable set of parameters J, F_j, G_j, p_j, q_j must be fixed. First consider a finite rectangle (indices $1 \le l \le N_x$ and $1 \le m \le N_y$) with β/k larger than the local refractive index. Since $\beta^2 - k^2\epsilon = \pm p_j^2 \pm q_j^2 > 0$, at least one of F_j and G_j must be the exp-function. As shown in Tab. 1(a), the set of trial functions can be divided into 12 subsets. Each is characterized by a choice for F_j and G_j and the signs of p_j and q_j. Possible transverse wave vectors (p_j, q_j) are located on a circle with radius $\sqrt{\beta^2 - k^2\epsilon}$ (for $(F,G) = (\exp,\exp)$) or a hyperbola (otherwise). Thus they may be prescribed by discrete values α_j chosen from a single parameter interval (see Tab. 1).

(a) $\beta^2 - k^2\epsilon > 0$, $w = \sqrt{\beta^2 - k^2\epsilon}$					**(b)** $k^2\epsilon - \beta^2 > 0$, $w = \sqrt{k^2\epsilon - \beta^2}$				
F	G	$\alpha \in$	p	q	F	G	$\alpha \in$	p	q
exp	exp	$]0, \pi/2[$	$w\cos(\alpha)$	$w\sin(\alpha)$	cos	cos	$]0, \pi/2[$	$w\cos(\alpha)$	$w\sin(\alpha)$
exp	exp	$]0, \pi/2[$	$w\cos(\alpha)$	$-w\sin(\alpha)$	cos	sin	$]0, \pi/2[$	$w\cos(\alpha)$	$w\sin(\alpha)$
exp	exp	$]0, \pi/2[$	$-w\cos(\alpha)$	$w\sin(\alpha)$	sin	cos	$]0, \pi/2[$	$w\cos(\alpha)$	$w\sin(\alpha)$
exp	exp	$]0, \pi/2[$	$-w\cos(\alpha)$	$-w\sin(\alpha)$	sin	sin	$]0, \pi/2[$	$w\cos(\alpha)$	$w\sin(\alpha)$
cos	exp	$]0, \infty[$	$w\sinh(\alpha)$	$w\cosh(\alpha)$	exp	cos	$]0, \infty[$	$w\sinh(\alpha)$	$w\cosh(\alpha)$
cos	exp	$]0, \infty[$	$w\sinh(\alpha)$	$-w\cosh(\alpha)$	exp	sin	$]0, \infty[$	$w\sinh(\alpha)$	$w\cosh(\alpha)$
sin	exp	$]0, \infty[$	$w\sinh(\alpha)$	$w\cosh(\alpha)$	exp	cos	$]0, \infty[$	$-w\sinh(\alpha)$	$w\cosh(\alpha)$
sin	exp	$]0, \infty[$	$w\sinh(\alpha)$	$-w\cosh(\alpha)$	exp	sin	$]0, \infty[$	$-w\sinh(\alpha)$	$w\cosh(\alpha)$
exp	cos	$]0, \infty[$	$w\cosh(\alpha)$	$w\sinh(\alpha)$	cos	exp	$]0, \infty[$	$w\cosh(\alpha)$	$w\sinh(\alpha)$
exp	cos	$]0, \infty[$	$-w\cosh(\alpha)$	$w\sinh(\alpha)$	sin	exp	$]0, \infty[$	$w\cosh(\alpha)$	$w\sinh(\alpha)$
exp	sin	$]0, \infty[$	$w\cosh(\alpha)$	$w\sinh(\alpha)$	cos	exp	$]0, \infty[$	$w\cosh(\alpha)$	$-w\sinh(\alpha)$
exp	sin	$]0, \infty[$	$-w\cosh(\alpha)$	$w\sinh(\alpha)$	sin	exp	$]0, \infty[$	$w\cosh(\alpha)$	$-w\sinh(\alpha)$

Table 1: Trial functions for a finite rectangle.

Tab. 1(b) gives the sets of trial functions for a finite rectangle if β/k is smaller than the local refractive index. Since now $k^2\epsilon - \beta^2 = \mp p_j^2 \mp q_j^2 > 0$, at least one of F_j and G_j must be a harmonic function.

The local coordinate offsets $x_{0,j}$, $y_{0,j}$ are introduced to meet symmetry requirements and to handle the exponential functions numerically. For rectangle $r = (l, m)$, if $F_j = \exp$ with $p_j > 0$ ($p_j < 0$) set $x_{0,j} = h_{x,l}$ ($x_{0,j} = h_{x,l-1}$). Otherwise, for $F_j = \sin$ or $F_j = \cos$, set $x_{0,j} = (h_{x,l} + h_{x,l-1})/2$. Analogously, $y_{0,j}$ is fixed in terms of $h_{y,m}$, $h_{y,m-1}$ depending on G_j and q_j.

For unbounded rectangles ($l = 0$ or $l = N_x + 1$, $m = 0$ or $m = N_y + 1$) Tab. 1 applies as well. Merely fields which are not square integrable over the rectangular domain must be dropped.

On corner rectangles, e.g. $l = 0$, $m = 0$, only one subset with outwards exponential decaying functions remains, provided that β/k is larger than the local refractive index. Otherwise no admissible subset would be left, thus no guided mode is possible. On the contrary, for rectangles unbounded in only one direction, both signs of $\beta^2 - k^2\epsilon$ yield valid subsets. The situation with β/k smaller than the local refractive index occurs frequently, e.g. if a rib has been etched from a guiding film as sketched in Fig. 1.

Now for each subset a number of discrete values α must be selected. Let N_α denote the maximum number. If only one of F and G is exponential, the parameter interval is not bounded. We introduced a largest admissible value $\alpha_{\max}$, which is set to $\pi/2$ if both F and G are exponential or harmonic functions. The selected values should be at least spaced by $\alpha_{\max}/N_\alpha$.

The selection starts with an arbitrarily prescribed value. We used $\alpha = 1$ if only one of F and G is exponential and $\alpha = \pi/4$ otherwise. It defines a trial function ϕ_α. The next parameter $\alpha \pm \Delta\alpha$ should yield a function $\phi_{\alpha+\Delta\alpha}$ which differs significantly from ϕ_α. A parameter d will limit this difference. The integrated deviation between the zero function and arbitrary linear combinations of the two functions should be larger than d:

$$\min_{a_1,a_2,a_1^2+a_2^2=1} \iint_r (a_1\phi_\alpha + a_2\phi_{\alpha+\Delta\alpha} - 0)^2 \, \mathrm{d}x \, \mathrm{d}y \geq d. \tag{6}$$

For normalized functions $\iint_r \phi_\alpha^2 \, \mathrm{d}x \, \mathrm{d}y = \iint_r \phi_{\alpha+\Delta\alpha}^2(x,y) \, \mathrm{d}x \, \mathrm{d}y = 1$ — this defines the normalization constants c_j introduced above — Eq. (6) reduces to

$$\Gamma_\alpha(\Delta\alpha) := \left| \iint_r \phi_\alpha \, \phi_{\alpha+\Delta\alpha} \, \mathrm{d}x \, \mathrm{d}y \right| \leq 1 - d. \tag{7}$$

Expansion of Γ_α results in a condition for the admissible parameter difference $\Delta\alpha$:

$$\Delta\alpha \geq \sqrt{\frac{d}{g(\alpha)}}, \quad \text{where} \quad g(\alpha) = -\frac{1}{2}\frac{d^2\Gamma_\alpha}{d\Delta\alpha^2}(0). \tag{8}$$

g is evaluated as a finite difference expression.

With this condition (8) and the constraint $\Delta\alpha \geq \alpha_{\max}/N_\alpha$ the values α_j can be selected, proceeding step-wise towards both ends of the parameter interval. This must be done seperately for each rectangle and each subset of trial functions. One obtains a spectral discretization with nonequidistant step sizes $\Delta\alpha$ on a spectral computational window $]0, \alpha_{\max}[$.

Since the trial value β enters this discretization procedure, it is carried out only once with an average value from each β interval under investigation. The parameter values α_j are stored, and for each trial value β the transverse wave vector components p_j and q_j are evaluated according to Tab. 1.

4   Joining the rectangles

For a given vector of amplitudes a_j^r the corresponding field will not satisfy the continuity requirements on the rectangle boundaries. The differences in the field and its normal derivative (possibly multiplied by the permittivity) are squared, summed, and integrated along the boundary lines. The resulting expression D measures the deviation of the field prescribed by $\{a_j^r\}$, β from a guided mode:

$$
\begin{aligned}
D_\beta(a_j^r) =\ & \sum_{l=0}^{N_x} \sum_{m=0}^{N_y+1} \int_{h_{y,m-1}}^{h_{y,m}} \left(O^{l+1,m}\Phi^{l+1,m} - O^{l,m}\Phi^{l,m} \right)^2 (h_{x,l}, y) \, \mathrm{d}y \\
+\ & \sum_{l=0}^{N_x} \sum_{m=0}^{N_y+1} \int_{h_{y,m-1}}^{h_{y,m}} \left(P^{l+1,m}\partial_x\Phi^{l+1,m} - P^{l,m}\partial_x\Phi^{l,m} \right)^2 (h_{x,l}, y) \, \mathrm{d}y \\
+\ & \sum_{l=0}^{N_x+1} \sum_{m=0}^{N_y} \int_{h_{x,l-1}}^{h_{x,l}} \left(Q_+^{l,m+1}\Phi^{l,m+1} - Q_-^{l,m}\Phi^{l,m} \right)^2 (x, h_{y,m}) \, \mathrm{d}x \\
+\ & \sum_{l=0}^{N_x+1} \sum_{m=0}^{N_y} \int_{h_{x,l-1}}^{h_{x,l}} \left(R_+^{l,m+1}\partial_y\Phi^{l,m+1} - R_-^{l,m}\partial_y\Phi^{l,m} \right)^2 (x, h_{y,m}) \, \mathrm{d}x.
\end{aligned}
\tag{9}
$$

Here, $h_{x,-1}$ and h_{x,N_x+1} are to be understood as $-\infty$ and $+\infty$, likewise for h_y. For the polarization dependent weighting factors O, P, Q, R we choose quantities as given by Tab. 2. With these weighting factors it is guaranteed that the continuity requirements on the boundary lines are satisfied if the error D is exactly zero.

	$O^{l,m}$	$P^{l,m}$	$Q_\pm^{l,m}$	$R_\pm^{l,m}$
QTE	1	$\dfrac{1}{k}$	$\dfrac{2\epsilon^{l,m}}{\epsilon^{l,m}+\epsilon^{l,m\mp 1}}$	$\dfrac{1}{k}$
QTM	1	$\dfrac{1}{\epsilon^{l,m}k}$	1	$\dfrac{1}{2k}\left(\dfrac{1}{\epsilon^{l,m}}+\dfrac{1}{\epsilon^{l,m\mp 1}}\right)$

Table 2: Weights for the least squares boundary error function.

However, the weighting factors are chosen somewhat arbitrarily — they may even be functions, but there is no a priori reason why they should. In a numerical calculation only a restricted set of trial functions is available, and the unknown mode function will usually not be included in the function space spanned by the trial functions. Therefore the minimum achievable error and consequently the estimate for the propagation constant depend on the choice of the weighting factors. However, if the set of trial functions is large enough, one can expect these dependence to vanish.

A similar ansatz (Least Squares Boundary Residual Method) has been applied successfully for the simulation of longitudinal waveguide discontinuities [32, 33, 34]. The authors used the freedom in the choice of the weighting factors to improve the conditioning of the resulting matrices (see section 5). We did not exploit this feature but merely introduced the factors $1/k$ and the permittivity averages in order to balance the influence on D between the field, its derivative, and between the contributions from horizontal and vertical boundaries.

Since D scales with the square of the coefficients a_j^r, only values D for normalized fields are to be compared. We used the expression

$$N_\beta(a_j^r) = \sum_{l=0}^{N_x+1}\sum_{m=0}^{N_y+1}\int_{h_{x,l-1}}^{h_{x,l}}\int_{h_{y,m-1}}^{h_{y,m}} c^{l,m}\left(\Phi^{l,m}(x,y)\right)^2 \mathrm{d}y\,\mathrm{d}x \tag{10}$$

for the squared field norm, with $c^{l,m}=1$ for QTE and $c^{l,m}=1/\epsilon^{l,m}$ for QTM polarization. The remark on the choice of D applies for N as well.

5 Numerical procedure

Inserting the modal field ansatz (4) into (9) and (10) and analytically evaluating the integrals reduces the expressions for the field error and norm to simple quadratic forms:

$$D_\beta(a_j^r) = \boldsymbol{a}^T\mathsf{D}_\beta\boldsymbol{a}, \qquad N_\beta(a_j^r) = \boldsymbol{a}^T\mathsf{N}_\beta\boldsymbol{a}, \tag{11}$$

where $\boldsymbol{a}$ denotes the vector of coefficients a_j^r and D_β and N_β are real sparse symmetric matrices. N_β has block-diagonal form, the sparsity pattern of D_β fits to the block structure of N_β. By construction, both D_β and N_β are positive.

While the latter statement holds mathematically, occasionally N_β turns out to be numerically indefinite: a few negative eigenvalues with small magnitude occur. This is due to an unnecessarily large set of trial functions on at least one rectangle. Some of these are numerically linearly dependent. (Note that the spectral discretization procedure considers only the difference between neighbored trial functions. Subsets of trial functions with different harmonic and exponential dependence are usually not orthogonal.) To restore positivity, one has to drop some of the trial functions. For each rectangle, we compute the smallest eigenvalue of the relevant part of the normalization Matrix N_β. If this value is negative, we drop the trial function with the largest amplitude in the corresponding eigenvector. This procedure is repeated until each block on the diagonal of N_β is positive.

We are left with the following minimization problem: For given β, find $\boldsymbol{a}$ with the smallest $\boldsymbol{a}^T D_\beta \boldsymbol{a}$, subject to the condition $\boldsymbol{a}^T N_\beta \boldsymbol{a} = 1$. This yields a generalized eigenvalue equation for the optimal coefficient vector:

$$D_\beta \boldsymbol{a} = \mu_\beta N_\beta \boldsymbol{a} . \tag{12}$$

The smallest eigenvalue μ_β must be calculated, which is the minimal achievable error. μ_β is minimized with respect to β, its minima yield approximations to the propagation constants. By insertion of the corresponding eigenvectors into (3), one finally obtains the modal fields.

To solve Eq. (12), we followed a strategy as outlined in [35]. Cholesky decomposition of the normalization matrix reduces Eq. 12 to an ordinary symmetric eigenvalue problem. The decomposition can be done separately for each diagonal block of N_β. Two subsequent backsubstitution steps take advantage of the block structure and the corresponding sparsity pattern of D_β as well, thus this part of the computation can be performed very efficiently. Afterwards we used the LAPACK-library [36] to find the lowest eigenvalue of the resulting ordinary eigenvalue equation.

Depending on the effort invested in the onedimensional minimization algorithm (see e.g. [35]), only very few evaluations of (12) are required. A good initial estimate for the propagation constant is helpful; we used WMM-calculations with a reduced number of trial functions for that purpose.

Many interesting structures show a mirror symmetry with respect to $y \rightarrow -y$, and their guided modes have a definite symmetry as well. In these cases the number of unknowns in the WMM calculations can be halved if one drops trial functions with unwanted symmetry in the centered rectangles. Additionally, each pair of corresponding coefficients on both sides must be treated as one unknown.

6 Results

6.1 Rib waveguides (I)

Tab. 3 summarizes the parameters of three sample rib waveguide geometries which have been widely used to compare different numerical methods for mode calculations [12, 13, 37, 7, 23, 22, 24, 21]. For Tab. 4, we extended the summary of previously published results from [21] by values from [37, 22, 24] and added a line with the WMM effective modal indices.

	n_s	n_f	n_c	w/μm	h/μm	t/μm
(i)	3.34	3.44	1.0	2.0	1.10	0.20
(ii)	3.36	3.44	1.0	3.0	0.10	0.90
(iii)	3.435	3.44	1.0	4.0	2.50	3.50

Table 3: Sample geometry parameters. The modeled vacuum wavelength was $\lambda = 1.55\,\mu$m.

For waveguides (i) and (ii) the WMM agrees remarkably well with the other approaches, especially with the supercomputer-results from [21] FDM$_2$, while for geometry (iii) the WMM modal indices are slightly larger. For waveguide (iii), note the perfect agreement between the WMM and the spectral index method SI. According to a remark in [21], a reason may be the limited computational window of the finite difference treatment (width in the y-direction: FDM$_1$: $12.7\,\mu$m with exponential decay [12], BPM$_1$, BPM$_2$, FDM$_2$: $16\,\mu$m with zero boundary condition [23, 22, 21]). Ref. [22] contains a figure with the corresponding *field* profile on the $16\,\mu$m window. The field looks like being squeezed between the window boundaries. Results from a variety of other vectorial and semivectorial methods concerning structure (i) are collected in [19]. The authors give the value 3.388687 for the QTE fundamental effective modal index, obtained by a fully vectorial finite difference calculation on a dense mesh. The WMM result deviates only in the sixth digit.

Fig. 2 shows intensity contours for the fundamental QTE and QTM modes. The reader may compare with the plots in [21]. There is good agreement, except the slightly wider spread WMM contours for guide (iii). The WMM-calculations for these structures were performed with equal parameters for the spectral discretization. We have set $\alpha_{\max} = 3$, $N_\alpha = 30$, and $d = 0.01$, for all rectangles and subsets of trial functions. This resulted in modal fields which are constructed from 887 (888), 890 (897), 854 (852) trial functions, for guides (i), (ii),

	QTE			QTM		
	(i)	(ii)	(iii)	(i)	(ii)	(iii)
FDM$_1$	3.38693	3.39544	3.43681	3.38674	3.39059	3.43677
SI	3.38874	3.39527	3.43690	3.38788	3.39032	3.43684
VM	3.38841	3.39544	3.43674	3.38766	3.39162	3.43668
BPM$_1$	3.38871	3.39547	3.43680	3.38792	3.39069	3.43677
BPM$_2$	3.38876	3.39556	3.43681	3.38799	3.39071	3.43677
BPM$_3$	3.38847	3.3958	3.4360	3.38865	3.3893	3.4367
FDM$_2$	3.38866	3.39534	3.43678	3.38787	3.39064	3.43674
WMM	3.38866	3.39527	3.43690	3.38780	3.39061	3.43685

Table 4: Modal effective indices β/k for the waveguides of Tab. 3. WMM-results are compared with previously published values (in chronological order): FDM$_1$: finite difference method by Stern [12], SI: spectral index method by Stern, Kendall and McIlroy [37], data from [22], VM: variational approach by Huang and Haus [7], BPM$_1$, BPM$_2$, BPM$_3$: finite difference beam propagation by Liu, Yang, and Yuan [23], by Liu and Li [22], and by Lee and Voges [24], FDM$_2$: finite difference approach by Noro and Nakayama [21].
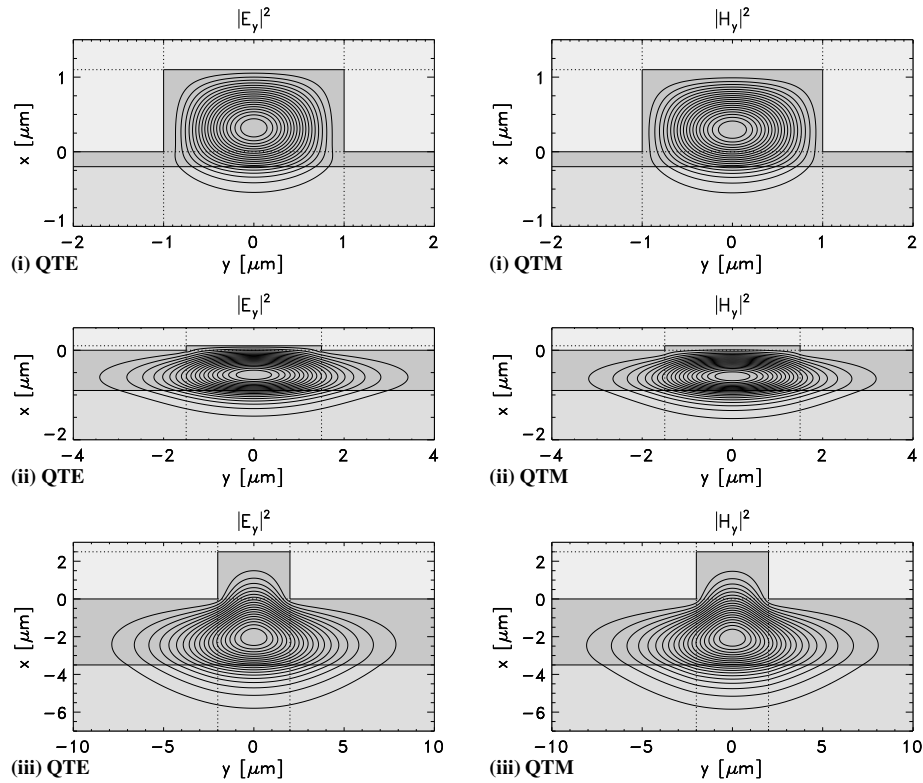

Figure 2: Modal field intensities for the sample structures with parameters of Tab. 3. Contour levels are spaced by 5% of the maximum field intensity. Note that the clippings from the waveguide cross section are chosen for displaying purposes only, the WMM fields are defined for the entire x-y-plane. Horizontal and vertical lines indicate the refractive index profile and its splitting into rectangular sections.

(iii) and QTE (QTM) polarization. For test purposes, symmetry with respect to $y = 0$ was *not* imposed by the selection of the trial functions. Coefficients for antisymmetric trial functions in the centered rectangles were computed approximately zero, while corresponding values on both sides of the symmetry plane turned out to be equal, as expected.

6.2 Rib waveguides (II)

Tab. 5 lists modal indices for another frequently investigated rib waveguide geometry [2, 10, 11, 12, 16, 17, 20]. It considers ribs of equal width, etched with varying depth from the same film. Again we found good agreement

t/μm	0.0	0.1	0.2	0.3	0.4	0.5	0.6	0.7	0.8
FEM$_1$	3.41200	3.41220	3.41235	3.41255	3.41285	3.41315	3.41365	3.41410	3.41475
FDM$_1$	3.41188	3.41200	3.41217	3.41240	3.41271	3.41310	3.41358	3.41415	3.41484
FEM$_2$	3.40970	3.40971	3.41003	3.41025	3.41057	3.41097	3.41148	3.41210	3.41298
FEM$_3$	3.41194	3.41209	3.41224	3.41247	3.41278	3.41312	3.41358	3.41414	3.41480
FDM$_2$	3.41200	3.41211	3.41226	3.41247	3.41275	3.41311	3.41355	3.41408	3.41472
WMM	3.41204	3.41214	3.41229	3.41250	3.41277	3.41312	3.41356	3.41409	3.41473

Table 5: QTE modal effective indices β/k for rib waveguides as sketched in Fig. 1 with parameters $w = 3.0\,\mu$m, $h = 1.0\,\mu$m $- t$, $\lambda = 1.15\,\mu$m, $n_s = 3.40$, $n_f = 3.44$, $n_c = 1.0$. FEM$_1$: vectorial finite element method by Rahman and Davies [11] (data from [20]), FDM$_1$: semivectorial finite difference method by Stern [12], FEM$_2$, FEM$_3$: vectorial finite element methods by Abid et. al. [16] and Koshiba et. al. [17], FDM$_2$: vectorial finite difference approach by Hadley and Smith [20]), WMM: the present method.
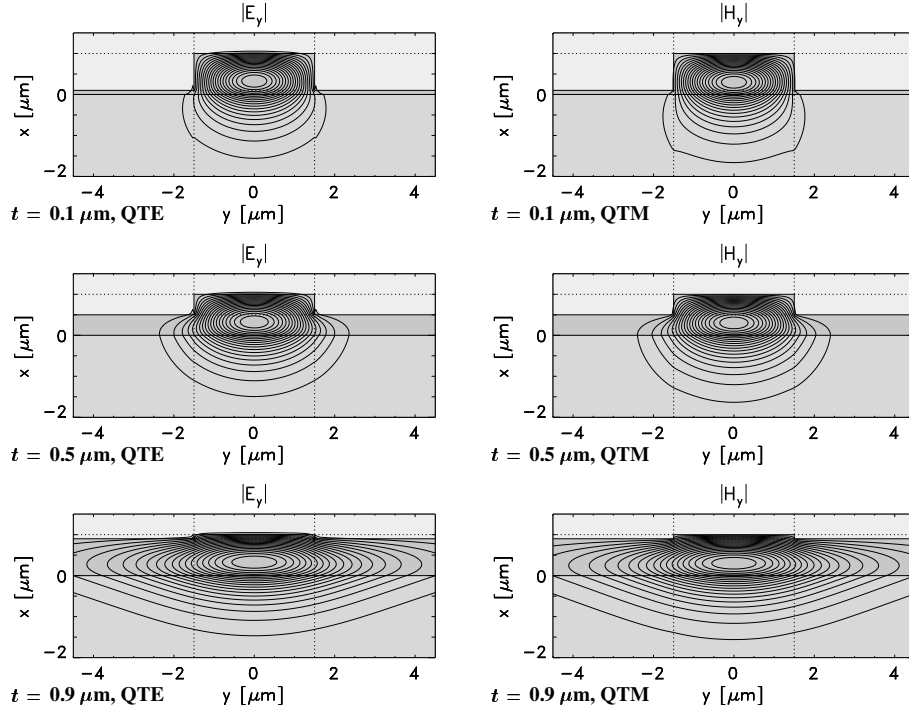

Figure 3: Fundamental modal fields for rib waveguides with varying etching depth (t: remaining film thickness) and parameters as given for Tab. 5. The contour levels are spaced by 5% of the maximum field.

between the WMM and previous methods, especially with the vectorial approach FDM$_2$ [20].

Some of the corresponding modal profiles are shown in Fig. 3. For larger etching depth, slight field irregularities remained close to the artificial rectangle boundaries in the substrate layer (if contours for $|E_y|^2$ were drawn, this would not be visible). Nevertheless, the fields look reasonable, the irregularities disappear with finer spectral discretization. The fields were calculated with parameters $\alpha_{\max} = 3$, $N_\alpha = 30$, and $d = 0.01$. Symmetry with respect to $y = 0$ has been explicitly imposed for this and all following examples. For $t = 0.5\,\mu$m, the depicted QTE modal function consists of 760 trial functions with 492 independent coefficients.

In a recent review article [2], these ribs with varying etching depth were chosen for a benchmark test. Among a variety of other vectorial and semivectorial approaches, the author considered the Modal Transverse Resonance Method MTRM [28] (Mode Matching Method) to be the most reliable for these waveguides. Tab. 6 compares effective modal indices from [2] with WMM values, normalized as $b = ((\beta/k)^2 - n_s^2)/(n_f^2 - n_s^2)$. Results from other methods regarded in [2] as reliable do not deviate by more than 0.001 from the MTRM. The WMM modal indices, computed with the moderate spectral discretization noted above, fall within this limit as well.

t/μm	QTE					QTM				
	0.1	0.3	0.5	0.7	0.9	0.1	0.3	0.5	0.7	0.9
MTRM	0.3019	0.3110	0.3270	0.3512	0.3883	0.2674	0.2751	0.2890	0.3107	0.3455
WMM	0.3024	0.3112	0.3268	0.3508	0.3881	0.2676	0.2759	0.2892	0.3102	0.3451

Table 6: Normalized modal effective indices b for rib waveguides with parameters as given for Tab. 5. MTRM: Results from the modal transverse resonance method by Sudbø, from [2].

6.3 Directional coupler

Two parallel rib waveguides on the same film may be regarded as the central part of a directional coupler device. In [21] such a coupler structure made of two waveguides of type (ii) in Tab. 3 has been investigated. Fig. 4 shows modal intensity contours for the ribs at a distance of $1\,\mu$m. We calculated $13.76627\,\mu\mathrm{m}^{-1}$ ($13.75944\,\mu\mathrm{m}^{-1}$) and $13.76427\,\mu\mathrm{m}^{-1}$ ($13.76217\,\mu\mathrm{m}^{-1}$) for the propagation constants β_s (β_a) of the symmetric (antisymmetric) supermodes for a waveguide separation of $1\,\mu$m and $3\,\mu$m, respectively. The corresponding coupling lengthes $\pi/|\beta_s - \beta_a|$ are 0.46 mm and 1.49 mm. This agrees well with the values of 0.45 mm and 1.47 mm given in [21].
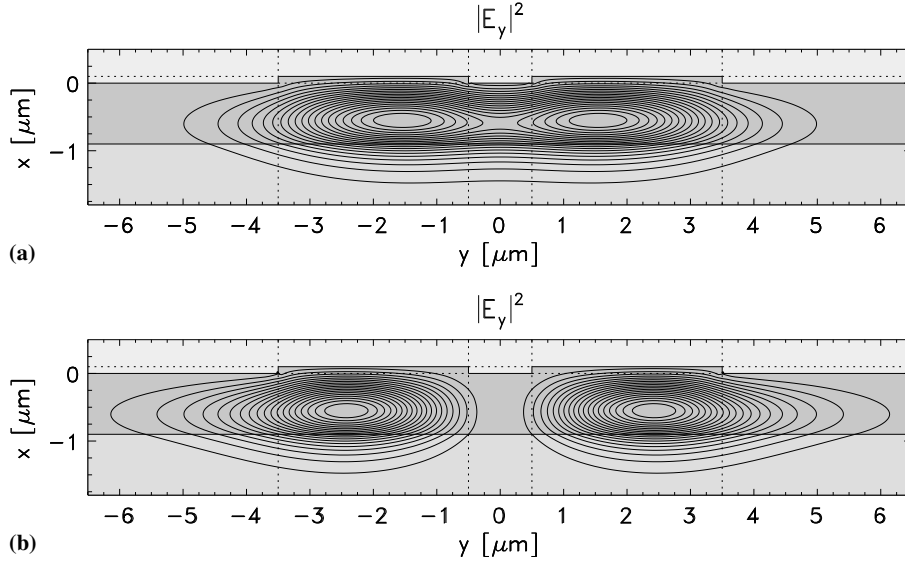

Figure 4: Intensity contours for the symmetric (a) and antisymmetric (b) fundamental QTE supermode of a directional coupler formed by two waveguides with the parameters of geometry (ii) in Tab. 3. Separation of the ribs is $1\,\mu$m.

6.4 Multimode waveguide

For the design of multimode-interference (MMI) devices [38, 39, 40, 41, 8, 42, 43, 34], a basic task is the exact calculation of propagation constants and modal fields for *all* guided modes of a multimode rib waveguide. Usually the effective index method is used (eventually combined with an approximate analytic expression for the propagation constants of a broad slab [38, 41]), but under certain circumstances deviations from this approximate approach become relevant [8]. To analyze higher order modes of broad rib waveguides with a rigorous finite difference or finite element method, the large waveguide cross section must be covered with a dense mesh, thus these simulations may be relatively expensive. The spectral index method has been employed [8], but it relies on vanishing fields on the rib surface, so it is of limited applicability. We will therefore consider a single multimode rib as the last example. Since the trial functions already exhibit the appropriate sinusoidal dependence in the guiding region, one can expect our method to yield good results with only a small number of unknowns.

Such a multimode structure serves best to illustrate the behaviour of the WMM error function. Fig. 5 shows the remaining error $D_\beta(a_j^r)$ in the field on the rectangle boundaries with the optimum vector of coefficients a_j^r inserted for each trial value β. The functions for symmetric and antisymmetric trial fields consist of sec-

tions with parabolic appearance, each centered around a propagation constant at its minimum. Thus after an initial bracketing the propagation constants can be fixed efficiently with only a very small number of function evaluations [35]. The domain with this piecewise-parabolic behaviour is limited by the propagation constant $10.11653\,\mu\mathrm{m}^{-1}$ of the corresponding planar waveguide. For larger β-parameters, the monotonous increase of both curves (as visible in Fig. 5) continues. The data were calculated with a spectral discretization given by $\alpha_{\mathrm{max}} = 3$, $N_\alpha = 30$, and $d = 0.01$.
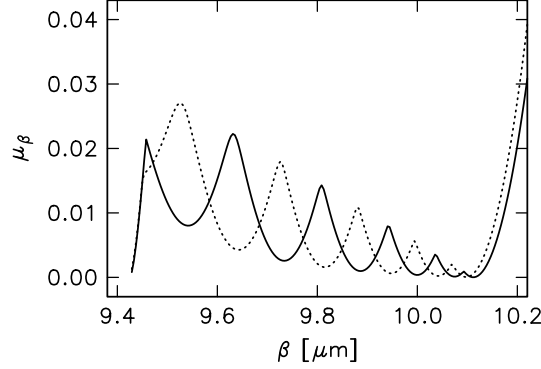
Figure 5: Dependence of the optimum field error μ_β on the trial value β for the analysis of a multimode rib waveguide Each minimum indicates a propagation constant. The continuous (dotted) line corresponds to symmetric (antisymmetric) QTM-polarized trial fields. We adopted a typical parameter set for magnetic garnets, a YIG rib on a GGG substrate [30]: $w = 10.0\,\mu\mathrm{m}$, $h = 0.5\,\mu\mathrm{m}$, $t = 0.0\,\mu\mathrm{m}$, $\lambda = 1.3\,\mu\mathrm{m}$, $n_s = 1.95$, $n_f = 2.3$, $n_c = 1.0$ (see Fig. 1).

For the totally etched structure ($t = 0$) the WMM has found 11 guided QTM-modes. As illustrated by Fig. 6, the dependence of the propagation constants on the mode number is well approximated [38, 41, 8] by the formula

$$ n_\nu = n_p - \frac{\lambda^2(\nu + 1)^2}{8 n_p w^2}, \tag{13} $$

where n_ν is the effective modal index of mode number ν and $n_p = 2.0931$ the effective index of the equivalent planar waveguide.
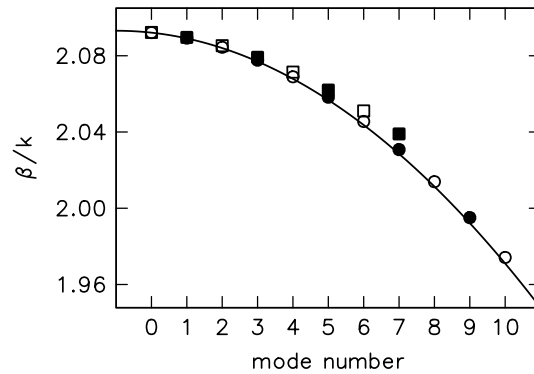

Figure 6: QTM effective modal indices of two multimode rib waveguides versus the number of zero lines of the mode function in the lateral direction. Circles indicate modal indices for a deeply etched structure with $h = 0.5\,\mu\mathrm{m}$, $t = 0.0\,\mu\mathrm{m}$, rectangles show values for a less confining waveguide $h = 0.1\,\mu\mathrm{m}$, $t = 0.4\,\mu\mathrm{m}$; other parameters are as given for Fig. 5. Open (filled) symbols correspond to symmetric (antisymmetric) modes. The line shows the levels given by Eq. (13).

According to Fig. 6 this simple expression is no longer valid for a less deeply etched rib. The modes are less confined and some of the higher order modes are cutoff, with the cutoff value given by the planar propagation constant of the outer slab of thickness t. The reader may compare with the more detailed discussion in [8].

Finally Fig. 7 shows a series of modal intensity plots for this structure. It should supply some evidence for the ability of the WMM to approximate fundamental as well as higher order modes.
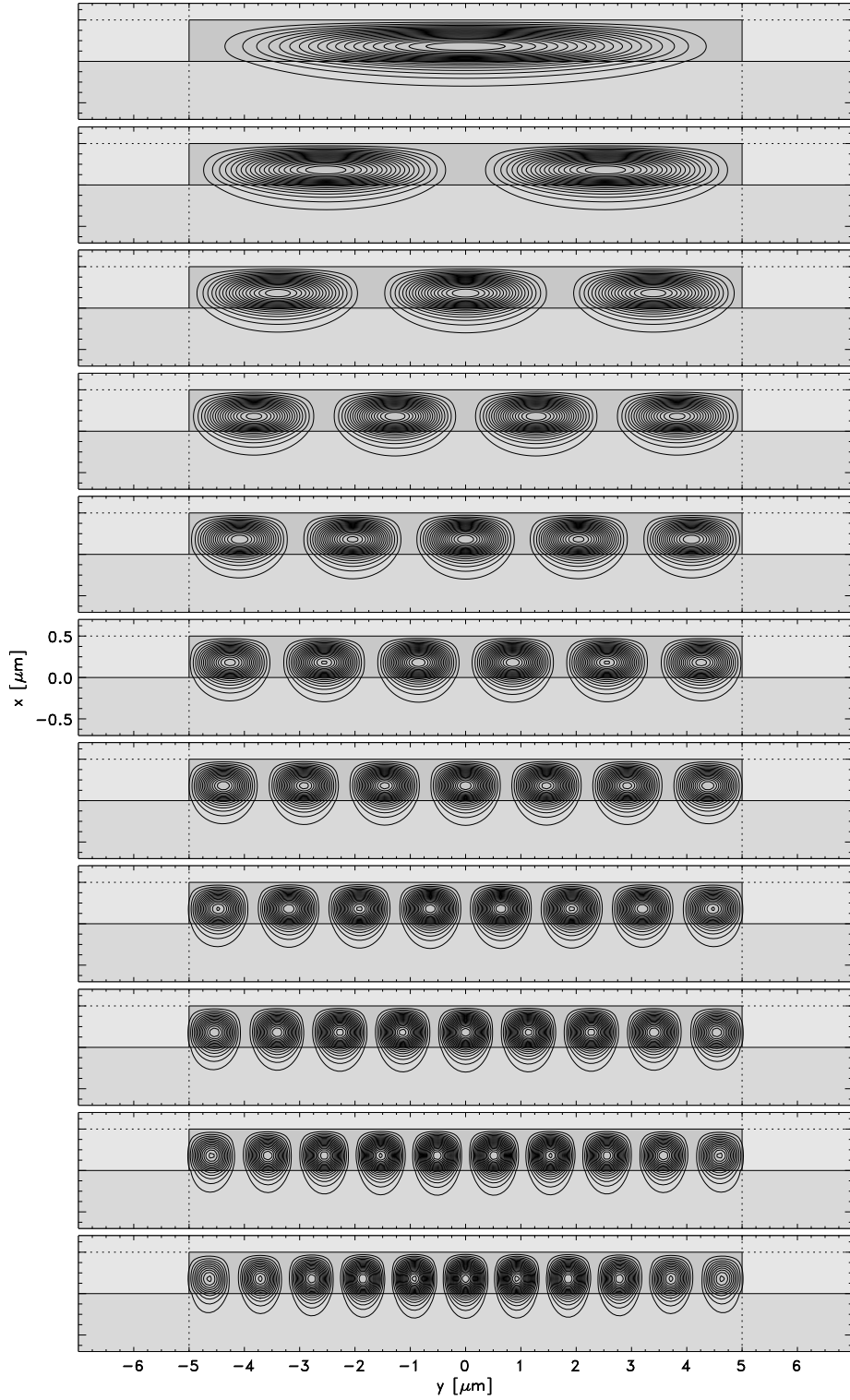
Figure 7: Field intensity plots for the guided QTM-modes of a broad rib waveguide as prescribed by the parameters of Fig. 5. The contours correspond to the square $\left|H_y\right|^2$ of the transverse magnetic field.

7 Conclusions

Obviously the simple linear combination (3) of factorizing trial functions (4) with exponential or harmonic dependence on the transverse coordinates forms a promising ansatz for the calculation of guided waveguide modes. Although convergence for dense spectral discretization is not proven, this function space turned out to be large enough to approximate the unknown exact modal fields well. Inside the homogeneous rectangles the trial functions solve Maxwells equations exactly. The field mismatch on the boundaries allows to determine the

propagation constants via minimization of a least squares quadratic form (9). For two widely established benchmark problems, we found excellent agreement between the WMM and several previously published methods.

The WMM shows to be quite economic both in computational time and memory consumption. Calculation of a single rib waveguide, e.g. the structure for $t = 0$ in Tab. 5, takes about one minute on a HP-9000/715 75 Mhz workstation for a program without special optimization effort, output of the modal field included. Memory is required for two matrices with a dimension of order 500 only; therefore the method is well qualified for an implementation on modern personal computers.

Frequently a mode solver forms only the basis of a more extensive tool for integrated optics design. Unlike methods based on finite differences or finite elements, the WMM yields continuous modal field representations which are defined on the entire plane of the waveguide cross section. They are therefore well suited for further processing, like calculation of overlap integrals, propagating mode analysis or evaluation of perturbation theory integrals (eg. [30]).

Although we restricted ourselves to the semivectorial analysis, extension of the WMM to vectorial calculations is possible. On each rectangle, two independent sets of trial functions are introduced to represent the two transverse electric or magnetic field components. The vectorial continuity relations for these components must be translated into a least squares expression. This approach avoids problems concerned with the diagonalization of nonsymmetric matrices for both vectorial and semivectorial calculations.

Acknowledgment

References

[1] K. S. Chiang. Review of numerical and approximate methods for the modal analysis of general optical dielectric waveguides. *Optical and Quantum Electronics*, 26:S113–S134, 1994.

[2] C. Vassallo. 1993-1995 Optical mode solvers. *Optical and Quantum Electronics*, 29:95–114, 1997.

[3] R. K. Varshney and A. Kumar. A Simple and Accurate Modal Analysis of Strip-Loaded Optical Waveguides with Various Index Profiles. *Journal of Lightwave Technology*, 6(4):601–606, 1988.

[4] A. Sharma, P. K. Mishra, and A. K. Ghatak. Single-Mode Optical Waveguides and Directional Couplers with Rectangular Cross Section: A Simple and Accurate Method of Analysis. *Journal of Lightwave Technology*, 6(6):1119–1125, 1988.

[5] P. N. Robson and P. C. Kendall, editors. *Rib Waveguide Theory by the Spectral Index Method*, New York, 1990. Wiley.

[6] T. Rozzi, G. Cerri, M. N. Husain, and L. Zappelli. Variational Analysis of the Dielectric Rib Waveguide Using the Concept of "Transition Function" and Including Edge Singularities. *IEEE Transactions on Microwave Theory and Techniques*, 39(2):247–257, 1991.

[7] W. Huang and H. A. Haus. A Simple Variational Approach to Optical Rib Waveguides. *Journal of Lightwave Technology*, 9(1):56–61, 1991.

[8] G. M. Berry and S. V. Burke. Analysis of optical rib self-imaging multimode interference (MMI) waveguide devices using the discrete spectral index method. *Optical and Quantum Electronics*, 27:921–934, 1995.

[9] K. S. Chiang. Analysis of the Effective-Index Method for the Vector Modes of Rectangular-Core Dielectric Waveguides. *IEEE Transactions on Microwave Theory and Technology*, 44(5):692–700, 1996.

[10] B. M. A. Rahman and J. B. Davies. Finite-Element Solution of Integrated Optical Waveguides. *Journal of Lightwave Technology*, 2:682–687, 1984.

[11] B. M. A. Rahman and J. B. Davies. Vector-H Finite-Element Solution of GaAs/GaAsAs Rib Waveguides. *IEE Proceedings*, 132(6):349–353, 1985.

[12] M. S. Stern. Semivectorial polarised finite difference method for optical waveguides with arbitrary index profiles. *IEE Proceedings, Pt. J*, 135(1):56–63, 1988.

[13] M. S. Stern. Semivectorial polarised H field solutions for dielectric waveguides with arbitrary index profiles. *IEE Proceedings, Pt. J*, 135(5):333–338, 1988.

[14] K. Bierwirth, N. Schulz, and F. Arndt. Finite-Difference Analysis of Rectangular Dielectric Waveguide Structures. *IEEE Transactions on Microwave Theory and Techniques*, MTT-34(11):1104–1113, 1986.

[15] U. Rogge and R. Pregla. Vectorial Method of Lines for the Analysis of Strip-Loaded Optical Waveguides. *Journal of the Optical Society of America B*, 8:459–463, 1991.

[16] Z.-E. Abid, K. L. Johnson, and A. Gopinath. Analysis of Dielectric Guides by Vector Transverse Magnetic Field Finite Elements. *Journal of Lightwave Technology*, 11(10):1545–1549, 1993.

[17] M. Koshiba, S. Maruyama, and K. Hirayama. A Vector Finite Element Method With the High-Order Mixed-Interpolation-Type Triangular Elements for Optical Waveguiding Problems. *Journal of Lightwave Technology*, 12(3):495–502, 1994.

[18] J.-Y. Su, P.-K. Wei, and W.-S. Wang. A New Iterative Method for the Analysis of Longitudinally Invariant Waveguide Couplers. *Journal of Lightwave Technology*, 12(12):2056–2065, 1994.

[19] P. Lüsse, P. Stuwe, J. Schüle, and H.-G. Unger. Analysis of Vectorial Mode Fields in Optical Waveguides by a New Finite Difference Method. *Journal of Lightwave Technology*, 12(3):487–493, 1994.

[20] G. R. Hadley and R. E. Smith. Full-Vector Waveguide Modeling Using an Iterative Finite-Difference Method with Transparent Boundary Conditions. *Journal of Lightwave Technology*, 13(3):465–469, 1995.

[21] H. Noro and T. Nakayama. A New Approach to Scalar and Semivector Mode Analysis of Optical Waveguides. *Journal of Lightwave Technology*, 14(6):1546–1556, 1996.

[22] P.-L. Liu and B.-J. Li. Semivectorial Helmholtz Beam Propagation by Lanczos Reduction. *IEEE Journal of Quantum Electronics*, 29(8):2385–2389, 1993.

[23] P.-L. Liu, S. L. Yang, and D. M. Yuan. The Semivectorial Beam Propagation Method. *IEEE Journal of Quantum Electronics*, 29(4):1205–1211, 1993.

[24] P.-C. Lee and E. Voges. Three Dimensional Semi-Vectorial Wide-Angle Beam Propagation Method. *Journal of Lightwave Technology*, 12(2):215–224, 1994.

[25] F. Wijnands, H. J. W. M. Hoekstra, G. J. M. Krijnen, and R. M. de Ridder. Modal Fields Calculation Using the Finite Difference Beam Propagation Method. *Journal of Lightwave Technology*, 12(12):2066–2072, 1994.

[26] F. Wijnands, T. Rasmussen, H. J. W. M. Hoekstra, J. H. Povlsen, and R. M. de Ridder. Efficient Semivectorial Mode Solvers. *IEEE Journal of Quantum Electronics*, 33(3):367–374, 1997.

[27] C. H. Henry and B. H. Verbeek. Solution of the Scalar Wave Equation for Arbitrarily Shaped Dielectric Waveguides by Two-Dimensional Fourier Analysis. *Journal of Lightwave Technology*, 7(2):308–313, 1989.

[28] A. S. Sudbø. Film mode matching: a versatile numerical method for vector mode fields calculations in dielectric waveguides. *Pure and Applied Optics*, 2:211–233, 1993.

[29] S. J. Hewlett and F. Ladouceur. Fourier Decomposition Method Applied to Mapped Infinite Domains: Scalar Analysis of Dielectric Waveguides Down to Modal Cutoff. *Journal of Lightwave Technology*, 13(3):375–383, 1995.

[30] M. Shamonin and P. Hertel. Analysis of nonreciprocal phase shifters for integrated optics by the Galerkin method. *Optical Engineering*, 34(3):849–852, 1995.

[31] H. J. W. M. Hoekstra. An Economic Method for the Solution of the Scalar Wave Equation for Arbitrarily Shaped Optical Waveguides. *Journal of Lightwave Technology*, 8(5):789–793, 1990.

[32] J. B. Davies. A Least Squares Boundary Residual Method for the Numerical Solution of Scattering Problems. *IEEE Transactions on Microwave Theory and Techniques*, MTT-21(2):99–104, 1973.

[33] B. M. A. Rahman and J. B. Davies. Analysis of Optical Waveguide Discontinuities. *Journal of Lightwave Technology*, 6(1):52–57, 1988.

[34] M. Rajarajan, B. M. A. Rahman, T. Wongcharoen, and K. T. V. Grattan. Accurate Analysis of MMI Devices with Two-Dimensional Confinement. *Journal of Lightwave Technology*, 14(9):2078–2084, 1996.

[35] W. H. Press, B. P. Flannery, S. A. Teukolsky, and W. T. Vetterling. *Numerical Recipes in C, 2nd ed.* Cambridge University Press, 1992.

[36] E. Anderson, Z. Bai, C. Bischof, J. Demmel, J. Dongarra, J. Du Croz, A. Greenbaum, S. Hammarling, A. McKenney, S. Ostrouchov, and D. Sorensen. *LAPACK Users' Guide, 2nd ed.* Society for Industrial and Applied Mathematics, Philadelphia, 1995.

[37] M. S. Stern, P. C. Kendall, and P. W. A. McIlroy. Analysis of the spectral index method for vector modes of rib waveguides. *IEE Proceedings, Pt. J*, 137:21–26, 1990.

[38] R. Ulrich and G. Ankele. Self-imaging in homogeneous planar optical waveguides. *Applied Physics Letters*, 27(6):337–339, 1975.

[39] J. M. Heaton, R. M. Jenkins, D. R. Wight, J. T. Parker, J. C. H. Birbeck, and K. P. Hilton. Novel 1-to-N way integrated optical beam splitters using symmetric mode mixing in GaAs/AlGaAs multimode waveguides. *Applied Physics Letters*, 61(15):1754–1756, 1992.

[40] L. B. Soldano, F. B. Veerman, M. K. Smit, B. H. Verbeek, A. H. Dubost, and E. C. M. Pennings. Planar Monomode Optical Couplers Based on Multimode Interference Effects. *Journal of Lightwave Technology*, 10(12):1843–1849, 1992.

[41] M. Bachmann, P. A. Besse, and H. Melchior. General self-imaging properties in N×N multimode interference couplers including phase relations. *Applied Optics*, 33(18):3905–3911, 1994.

[42] L. B. Soldano and E. C. M. Pennings. Optical Multi-Mode Interference Devices Based on Self-Imaging: Principles and Applications. *Journal of Lightwave Technology*, 13(4):615–627, 1995.

[43] C. M. Weinert and N. Agrawal. Three-Dimensional Finite Difference Simulation of Coupling Behaviour and Loss in Multimode Interference Devices. *IEEE Photonics Technology Letters*, 7:529–531, 1995.